Chapter 8
Colloidal Microrobotic Swarms

Qian Zou, Yibin Wang and Jiangfan Yu

8.1 Introduction

Swarms consisting of living animals widely exist throughout nature. Various types of patterns and structures are formed by thousands or even millions of individual creatures, purely through local communications, such as bacteria colonies, bird flocks and insect swarms. These animals can change their swarm patterns through communication, in order to adapt to the ambient environments they interact with. In the past two decades, researchers are dedicated in developing robotic swarms by learning from natural swarm intelligence, aiming to realize complex tasks that are overwhelming for a single robot. It is well known that macroscale robotic swarms have been applied in many areas, including cargo allocation, terrain mapping and entertainment industry, and the small-scale swarms consisting of a large number of microrobotic agents can also play important roles in critical areas, such as biomedicine.

The actuation and control strategies for individual untethered microrobots were developed two decades ago. Driven by external physical fields, microrobots are capable of performing complex tasks at the microscale, such as micromanipulation, targeted drug delivery and even biopsy [1–3]. Drugs or cells (e.g. stem cells) can be loaded onto microrobots, and using external fields, they are navigated to pass through constrained environments towards targeted locations for in vivo localized

Q. Zou · Y. Wang
School of Science and Engineering, The Chinese University of Hong Kong, Shenzhen, Shenzhen, China

J. Yu (✉)
School of Science and Engineering, The Chinese University of Hong Kong, Shenzhen, Shenzhen, China

Shenzhen Institute of Artificial Intelligence and Robotics for Society, Shenzhen, China
e-mail: yujiangfan@cuhk.edu.cn

Y. Sun et al. (eds.), *Field-Driven Micro and Nanorobots for Biology and Medicine*, https://doi.org/10.1007/978-3-030-80197-7_8

therapies [4–8]. However, the capacity of loading drugs, in vivo imaging feedback signal strength, the capability of resisting flow and motion dexterity of an individual microrobot may meet critical limitations, owing to the constraints of their small sizes and volumes. Therefore, microrobotic swarms begin to attract worldwide extensive attention recently. By applying swarm control, drug dose that can be delivered at one time increases significantly [9, 10], and feedback signal of medical imaging systems [11], motion dexterity and robustness against external disturbances can be enhanced.

To date, to realize pattern control and motion control of a microrobotic swarm is still challenging [12–15], due to the inaccessibility of integrating onboard processors, sensors and actuators onto each of microrobotic agents. Therefore, the physical and/or chemical among the agents needs to serve the role of "wireless communication" [16], which still requires further investigation. Colloidal systems are ideal simplified models to study swarm behaviours, because the systems are homogeneous, the agents are isotropic, and the agent-agent interactions can be modelled. To date, progresses have been made. Generating a stable pattern is the first step in swarm pattern control. Previously, it has been reported that functionalized Janus particles could self-assemble into complex predefined lattices or synchronization-selected microtubes [17–19]. Controllable and reversible process of forming ribbon-like and ring-like structures, using colloidal silica rods coated with hemicylindrical magnetic layers, have been reported [20]. In addition, optical fields [21, 22], ultrasound [23], magnetic fields [24, 25] and chemical signaling [26] are capable of triggering formation of microrobotic swarm behaviours.

After forming a stable swarm pattern, how to control its motion is another critical issue. Magnetic fields are widely used for the motion control of microrobotic swarms, due to its high precision, high response frequency and good penetration to biological tissues. By forming a dynamically stable swarm and realizing its translational locomotion as an entity, the targeting rate of delivery, motion flexibility and controllability can be enhanced. It has been reported that magnetic microparticles exhibited spontaneous formation of dynamic localized snake-like patterns in an alternating magnetic field [27]. The pattern was formed on a liquid-air interface, and its motion is controllable. After 2017, the controllability of microrobotic swarm features, e.g. generation, pattern reconfiguration and motion control, has been significantly improved [28–30]. Two major research purposes are focused with the development of microrobotic swarms, i.e. fundamental investigation for guiding principles and rules that govern the swarm behaviours [31], and developing promising swarms that are practical for different applications, especially biomedical applications, such as minimally invasive surgeries [32, 33].

In this chapter, we will firstly summarize swarm behaviours driven by different external physical fields, including magnetic, electric, optical and acoustic fields. In addition, swarms triggered by chemical signaling will also be reviewed. Then, we will focus on two types of magnetic field-driven swarms, i.e. vortex-like swarms and ribbon-like swarms. The governing principles, control strategies and potential biomedical applications will also be reviewed.

8.2 Field-Driven Microrobotic Swarms

Swarm behaviours of micro-/nanorobots driven by magnetic fields have been intensively investigated. Tiny structures, such as magnetic particles, nanorods, helices and magnetotactic bacteria, have been used as microrobotic agents for swarms. Magnetic fields have fast response to input current, are easy to be tuned on-demand and have good penetration to biological tissues. Magnetotactic bacteria (MTB) with flagella can perform locomotion at low Reynolds number fluids, and due to the magnetosome chains inside their bodies, their moving direction can be controlled by tuning external magnetic fields. A swarm of MC-1 bacteria gathered using magnetic field gradients could perform micromanipulation and assembly of complex planar structures in fluids (Fig. 8.1A1), indicating the high precision of magnetic field-driven swarms [15]. The colloidal asters from suspended magnetic microparticles could be formed at liquid-liquid interfaces (Fig. 8.1A2), under a high-frequency oscillating magnetic field. The aster-like swarms could perform reversible pattern opening/closing and targeted locomotion. Similarly, the field can also trigger the formation of snake-like swarms. They spontaneously broke the symmetry of surface flow and generated asymmetric vortices at their tips, and thus, they were capable of propelling themselves (Fig. 8.1A3). Recently, the patterns of particle swarms floating at an air-liquid interface could be controlled in a time-varying manner, using arrays of permanent magnets [34]. The equilibrium of magnetic interactions and surface tension was reached, which resulted in the swarm pattern generation (Fig. 8.1A4). The swarms were capable of passing through complex and confined environments and were highly reconfigurable for cooperative manipulation tasks.

Electric fields can trigger swarm behaviours of polarized agents. The generation of electric field-driven swarms is significantly influenced by the electrical properties of the agents and their surround media. In general, the mechanisms of the swarm behaviours can be categorized into two types, i.e. electrostatic interactions and electrohydrodynamics. Yan et al. reported various collective states of metal-dielectric Janus colloids were reconfigured by introducing electrostatic imbalance (Fig. 8.1B1) [35]. The phenomenon was caused due to the different polarization of metal and dielectric hemispheres colloids in AC electric fields. Dipolar interactions between particles were negligibly weak at low frequencies (~kHz), due to strong ionic screening effects. In this state, the particles were in a gas-like state. At moderate frequencies (20–50 kHz), ionic screening effects were reduced, and the dipolar repulsion between metallic hemispheres led to the formation of coherent swarms. At MHz-level frequencies, ions barely responded to high-frequency oscillating field, and thus the particles formed chains through head-to-tail dipolar interactions. In a sufficiently high-strength DC electric field, a kind of electrohydrodynamics phenomenon, i.e. Quincke rotation, will be induced when particles are less conductive compared with their surrounding liquid. The curved trajectories of the rolling particles resulted from their asymmetric shape, and the trajectory curvature was related with the applied electric field strength (Fig. 8.1B6). At a low particle

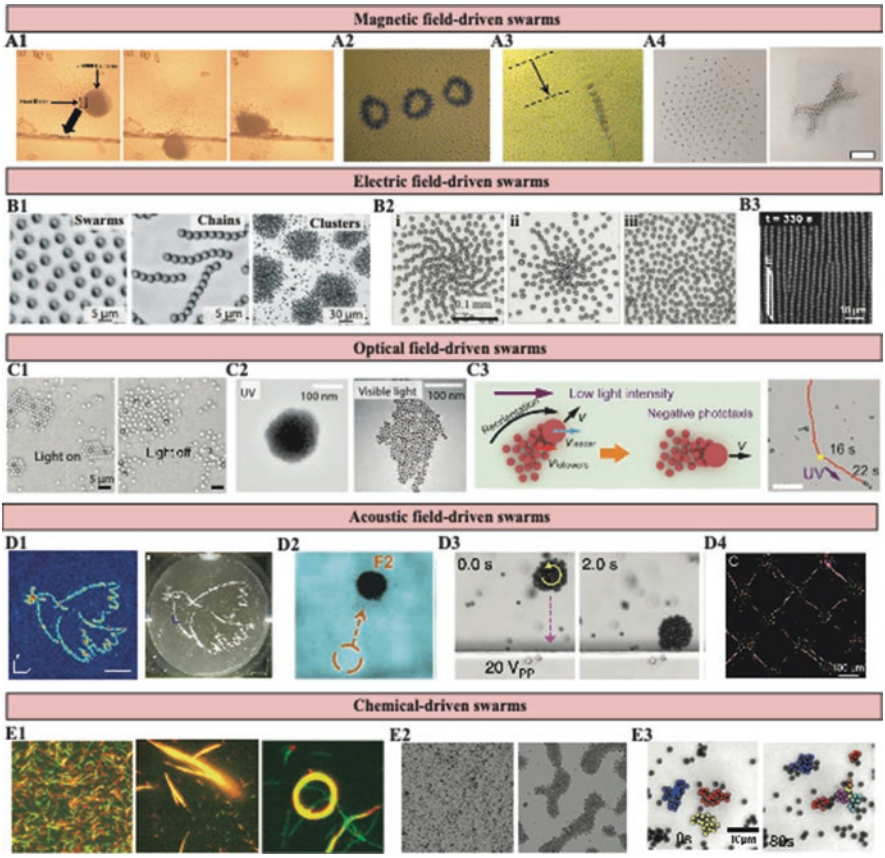

Fig. 8.1 (**A**) Magnetic field-driven swarms. (**A1**) Micromanipulation using a swarm of magnetotactic bacteria [15]. (**A2**) Self-assembled magnetic asters formed at a liquid-liquid interface [10]. (**A3**) Self-propulsion of a snake-like swarm [27]. (**A4**) Pattern formation of microrobots on a liquid-air interface driven by permanent magnets [34]. (**B**) Electric field-driven swarms. (**B1**) Swarms, chains and clusters formed by Janus particles [35]. (**B2**) Local ordering of pear-shaped particles in (*i*) "heads-out" vortex, with the particles oriented away from the vortex centre; (*ii*) "heads-in" vortex, with the particles oriented towards the vortex centre; and (*iii*) rotating flocks, with the particles synchronously pointing in one direction while the flock itself rotates [36]. (**B3**) Formation of sheet-like and chain-like patterns of polymer particles in electric fields [37]. (**C**) Optical field-driven swarms. (**C1**) Active TiO_2/SiO_2 Janus particles and passive silica particles form reversible crystal patterns due to the catalytic decomposition of hydrogen peroxide under UV light [38]. (**C2**) Reversible aggregation of functionalized gold nanoparticles induced by UV light, due to photoisomerization, which disassembles by applying visible light [39]. (**C3**) Negative and positive phototaxis of a hierarchical swarm at low and high UV light intensity, respectively [40]. (**D**) Acoustic-driven swarms. (**D1**) By applying a 3D-printed transmission hologram, desired phase information is encoded onto the hologram surface, and precise micromanipulation can be realized [41]. (**D2**) Controlled movement of a nanomotor swarm [23] . (**D3**) A particle swarm formed by a rotating magnetic field can move towards a wall in an acoustic field [42]. (**D4**) Experimental results of SSAW-assisted nanowire patterning technique [43]. (**E**) Swarms triggered by chemical signaling. (**E1**) Linear and circular swarms can be formed using rigid and soft DNA-functionalized microtubes, respectively, with the presence of linker DNA [44]. (**E2**) Reversible generation of gold microparticle swarms induced by adding or removing hydrazine [26]. (**E3**) Dynamic swarming of self-propelled gold colloids with half-spherical platinum covers. The coloured particles indicate the exchanges between different clusters [45]

concentration, the particles formed a vortex swarm. They aligned their directions away from the vortex centre when electric field strength was lower while pointing towards the centre when the strength was higher. With a high particle concentration and a strong field strength, the particles formed rotating flocks. Charged polymer spheres exhibited different crystalline phases, due to the counterbalance between charge repulsion and dipolar attractions (89). Applying a uniaxial and a biaxial electric field, the particles were further self-assembled into strings (1D) and sheets (2D), respectively (Fig. 8.1B3) [37].

Microrobotic agents with light-sensitive properties can form swarms under specific optical stimuli. Local ionic concentration gradient induces diffusiophoretic attraction to trigger swarm behaviours, e.g. the assembly of passive silica particles onto active TiO_2/SiO_2 Janus particles to form dynamic crystals (Fig. 8.1C1) [38]. One of the key principles for assembling functionalized gold nanoparticles is photoisomerization of azobenzene. Few azobenzene ligands can be decorated onto nanoparticles to enable their reversible formation of metastable crystals with the illumination of UV and visible light (Fig. 8.1C2). In addition, a high concentration of azobenzene ligands resulted in irreversible and permanently cross-linked structures [39]. Phototaxis is an intelligence existing in many natural creatures. Light-driven swarms mimicking phototactic behaviours have been reported recently. A hierarchical swarm consisting of a large TiO_2 particle and several small SiO_2 particles exhibiting positive or negative phototaxis was demonstrated, which depended on the direction and intensity of the applied UV light (Fig. 8.1C3) [40]. The particle swarm stopped moving or exhibited phototactic characteristics when UV light was vertical to the experimental plane or applied sideways, respectively.

Acoustic fields can also trigger swarm behaviours of microrobotic swarms. Through modifying acoustic waves, holographic techniques were applied for complex patterning of microrobotic agents (Fig. 8.1D1) [41]. A 3D-printed transmission element whose material had a sound transmission speed different from the surrounding medium was made for the hologram. The special structure reconstructed diffraction-limited acoustic pressure fields and changed the ultrasound waves. Manipulation with a precision at the microscale and assembly of particles into arbitrary static patterns were realized assisted by acoustic holograms. Reversible assembly and controlled movement of chemically powered nanomotor swarms were demonstrated (Fig. 8.1D2) [23], as well as the separation of spherical Janus motors and Au-Pt nanowires. The applied acoustic pressure exerted by the acoustic fields is the main reason for the migration of the nanomotor swarms. By tuning the acoustic frequency, the moving direction can be controlled as well. Ahmed et al. reported the neutrophil-inspired propulsion of superparamagnetic microparticle swarms in a channel (Fig. 8.1D3) [42]. Superparamagnetic microparticles experienced dipole-dipole interactions and aggregated into spinning swarms in a rotating magnetic field. Acoustic fields were applied in order to provide forces to pull the swarms to a solid boundary. Due to the wall effect, i.e., the viscosity near a solid boundary is larger than that far from it, the swarm was moved along the wall. Besides acoustic field gradient, standing surface acoustic wave (SSAW) was also used for nanopatterning tasks. Dispersed nanowires in suspension and on solid substrate can be

tuned to form patterns using SSAW [43]. The vibrations caused by SSAW induced a nonuniform charge distribution on the substrate, which generated electric fields from positive charges to negative charges. Because of dielectrophoresis effect, the metallic nanowires were aligned and patterned, e.g. parallel and perpendicular arrays (Fig. 8.1D4).

Besides the aforementioned physical interactions, chemical signaling is also an important method for regulating interactions among agents for swarm formation. Chemical-based or molecular-based binding, such as antibody-antigen and DNA-based binding, is highly selective. DNA-functionalized microtubes can move on a kinesin-coated substrate with the presence of adenosine triphosphate (ATP) [44]. When linker DNA was added, the microtubes moved towards each other and formed swarms with increasing sizes (Fig. 8.1E1). The larger swarms maintained their translational motion with a velocity close to that of individual microtubes. When flexible microtubes were applied, the swarms will perform circular motion, which has no crosstalk with mixed rigid microtubes, indicating the high selectivity of DNA-based linking. The concentration gradient of electrolytes enables ion exchanges, and in some cases, the diffusion coefficients (i.e. diffusing speed and diffusivity) of cations and anions are different. Therefore, a local electric field is generated, resulting in electrophoretic motion of the particles and electroosmotic motion of the fluid. Hydrazine can trigger reversible swarm behaviours of gold microparticles in hydrogen peroxide solution (Fig. 8.1E2) [26]. The reaction between hydrogen peroxide and hydrazine was catalysed by gold surface, and H^+, $N_2H_5^+$ and OH^- were generated. The induced local electric field acted phoretically on the nearby gold particles (i.e. electrophoretic motion), pulling them towards the highest electrolyte concentration (centre of the swarm). Meanwhile, electroosmotic effect also pumped the fluid towards the particles. The combination of these two effects resulted in the formation of particle swarms. Gold microparticles half-coated with platinum layers will dynamically cluster with the presence of hydrogen peroxide (Fig. 8.1E3) [45]. Upon the addition of H_2O_2, particle clusters coexisting with spread particles (gas phase) appeared. The clusters dynamically merged and disassembled with particles moving in and out.

8.3 Vortex-Like Swarms

In order to realize the formation of colloidal swarms, two critical types of interactions can be utilized, i.e. medium-based interactions and field-induced agent-agent interactions. Medium-based interactions indicate the interactions exerted via fluid, interface and boundaries, while agent-agent interactions indicate the interactions exerted among different agents.

As our previously published results [30], theoretically, paramagnetic nanoparticles are likely to perform a chain structure by attracting the adjacent particles. Thus, the nanoparticle chain is considered as the minimum block in the following analysis. This minimum unit will generate a local fluidic vortex. Figure 8.2 shows

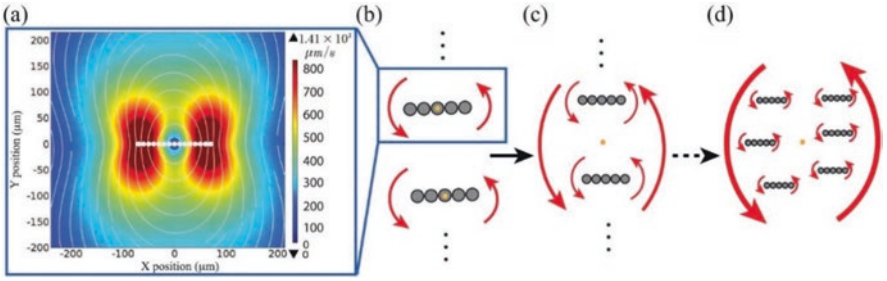

Fig. 8.2 Merging process of the vortices. (**a**) Local flow induced by a rotating particle chain with a frequency of 5 Hz, while the magnitudes of velocity field are illustrated by colour profile. (**b**)–(**d**) Paramagnetic nanoparticles are indicated by the grey circles, the red arrows represent induced velocity flows, the thicker red arrows denote vortex flows with higher velocity magnitude, and the yellow spots are the co-rotating centres of these chains

simulation results of this process. As shown in Fig. 8.2a, the flow velocity near two edges is higher than those near the centre where the velocity magnitude of flow is zero. The velocity field induced by individual rotating chains is shown by white lines. The following formula presents the vorticity $\vec{\xi}$ of a flow field:

$$\vec{\xi} = \nabla \times \vec{\mu} = \left(\frac{\partial u_z}{\partial y} - \frac{\partial u_y}{\partial z}, \frac{\partial u_x}{\partial z} - \frac{\partial u_z}{\partial x}, \frac{\partial u_y}{\partial x} - \frac{\partial u_x}{\partial y} \right) \tag{8.1}$$

where $\vec{\mu}$ denotes velocity distribution and u_x, u_y and u_z are the three components of $\vec{\mu}$ along the three axes of Cartesian coordinates. If the flow is confined in a two-dimensional vortex, Eq. (8.1) can be simplified as follows:

$$\vec{\xi} = \left(\frac{\partial v_y}{\partial x} - \frac{\partial v_x}{\partial y} \right) \vec{z} \tag{8.2}$$

According to its definition, circulation Γ is the line integral around a closed curve of the velocity field. Thus, it can be presented as:

$$\Gamma = \oint_c \vec{u} \mathrm{d}l = \int_A \vec{\xi} \cdot \vec{n} \mathrm{d}s \tag{8.3}$$

where A represents a reducible closed surface and C is the surface contour. The relationship between vorticity and the angular velocity of the vortex ω can be mathematically shown as $\xi = 2\omega$. VPNS is regarded as the core region of the vortex with a rigid rotation. Thereby, we can estimate the vorticity of VPNS.

8.3.1 Vortices Merging

The merging process of vortices which is induced by the rotating particle chains strictly determines the generation of a VPNS, as depicted in Fig. 8.2b–d. Firstly, the particle chains are dispersed in the fluid. They rotate around their chain centre when they are subjected to a rotating magnetic field, which leads to a vortex. This vortex generates long-range attracting forces which attract the adjacent chains. Therefore, the distances between each chains are reduced compared with original distance. Once the distance between two rotating chains is lower than a predefined threshold, they rotate around the same axis, and they begin to merge. Figure 8.2b, c shows the schematic illustration of the merging process. The pair of chains rotates around their centre. The thicker red arrows in Fig. 8.2c represent a stronger flow field after the merging of two vortices. Moreover, the vortex generated by the pair chains can also merge with other vortices, which leads to a huge system with dynamic equilibrium. This means more larger vortices will be generated after merging. In the internal part of a stable VPNS, the schematic depiction of forces exerted on *i*th chain is displayed in Fig. 8.3. These forces include a repulsive fluidic forces F_{i+1}^{v} induced by short-range interaction within two vortices, a magnetic repulsive force F_{i+1}^{r} induced by $i + 1$th chain and an internal force F_i^{a} inwardly generated by the vortex flow. The resultant force of the three dynamical-equilibrium forces is a centrifugal force which enables the rotation of the *i*th chain around the swarm centre.

If the separation distance d between two vortices is larger than the vortex core radius a, a slow viscous revolution is performed. Specifically, if the ratio of vortex core radius and distance is equal to a critical value $(a/d)_c = 0.3$, the merging process of vortices starts. The value of proposed ratio a/d will determine this merging process. Figure 8.4 shows a simulated merging phenomenon of two vortices and the distribution of two identical vortices. The advection of vorticity which is also known as the long-range attractive interaction propels the motion of vortices at the beginning. They move towards each other and instantly deformed into prolate shapes when two vortices begin to contact. Simultaneously, a diffusion phenomenon drives the vorticity field into one distribution, which is depicted in Fig. 8.4b. Figure 8.4c illustrates a third stage where the vortices coalesce into an elliptical shape and two strong filaments of vorticity eject. As shown in Fig. 8.4d, a circular axisymmetric vortex is produced in the final stage. Meanwhile, the filaments steadily roll up around the vortex core and dissipate. The simulation results can strongly support the hypothesis of merging phenomenon and VPNS generation.

8.3.2 Minimum Particle Concentration of Generating a VPNS

The minimum particle concentration to generate a VPNS is easily estimated with a known critical value $(a/d)_c$. The total mass M is computed as $M = C_0V_0$, where C_0 is original suspension and V_0 indicates the volume. Thus, the total volume of

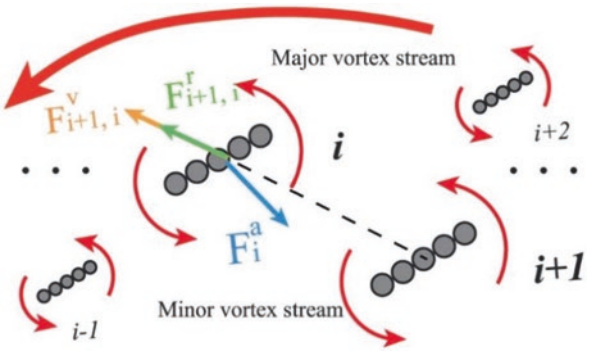

Fig. 8.3 Interaction forces exerted on the *i*th chain by the $i + 1$th chain. The blue arrows are the inward fluidic force exerted by the major vortex stream, the yellow arrows denote a repulsive force by the short-range vortex-vortex interaction, and the green arrows represent a repulsive magnetic force

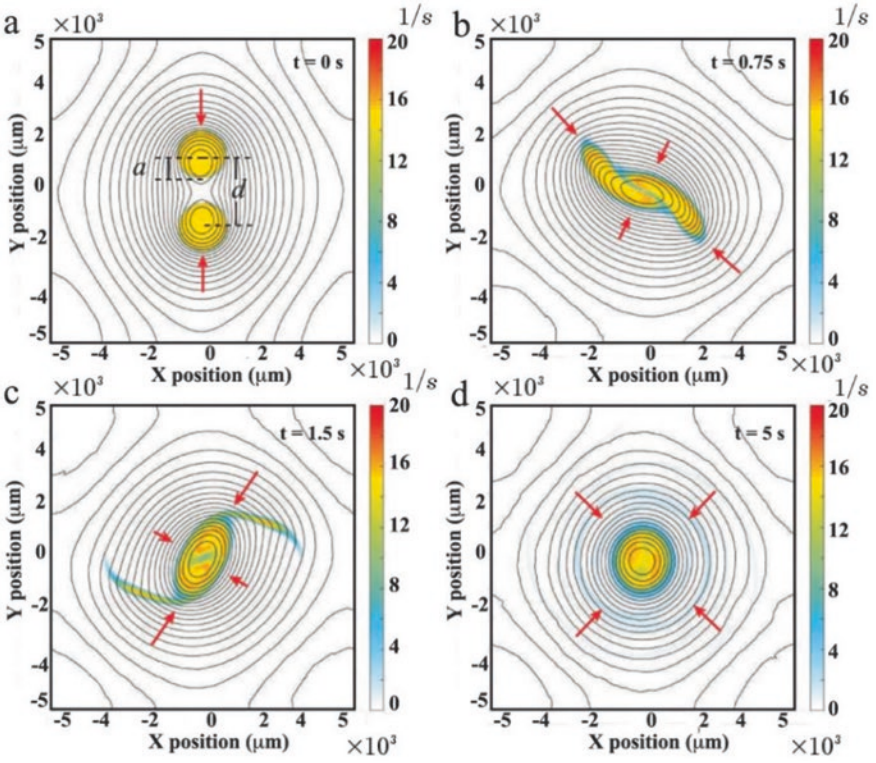

Fig. 8.4 Simulation results of the merging process of two identical vortices. The vorticity field is shown using the colourmap. Initially, $a/d = 0.3$, vortices radius is 800 μm, and vorticities distribution is uniform. a denotes the core radius of each vortex, while d indicates the relative distance between two vortices. The direction of fluidic pressure at the points is illustrated by red arrows

Table 8.1 Key parameters used in the calculation of the minimum nanoparticle concentration for generating a VPNS

Parameter	Value
C_o	4.5 μg/μl
V_o	12 μl
ρ	5180 kg/m^3
r_c	5 μm
h	50 μm
$(a/d)_c$	0.3

nanoparticles is $V_p = M/\rho$, with the density of magnetite ρ. Then, the average volume of each nanoparticle chain is estimated using $V_c = \pi r_c^2 h$; here, r_c is cross-section radius, and h implies an estimated height with a Mason number model at 10 Hz [46]. Therefore, the total number of nanoparticle chains is computed as $N_c = V_o/V_c$ under an assumption that the chains are uniformly and densely distributed. Finally, the minimum nanoparticle concentration is calculated to be 3.2 μg/mm^2 using these parameters in Table 8.1.

8.4 Characteristics of a VPNS

It is significantly important to investigate the characteristics of a VPNS for tough robotics tasks. Those characteristics include the motion equation and the fluidic interactions inside or outside the vortex core. Before introducing the equation of motion, the momentum equation in an internal frame of reference is expressed as follows:

$$\frac{D\vec{u}}{Dt} = \frac{\partial \vec{u}}{\partial t} + \left(\vec{u}\cdot\nabla\right)\vec{u} = \frac{-\nabla P}{\rho} + \frac{\nabla\cdot\tau}{\rho} + \vec{g} \tag{8.4}$$

where $\vec{u}$ is flow velocity distribution, P denotes a local pressure, ρ is a local fluid density, τ is stress tensor, D/Dt represents Lagrangian derivative, and the body forces per unit mass are indicated as $\vec{g}$. Equation (8.4) can be rewritten as:

$$\frac{\partial \vec{u}}{\partial t} + \nabla\left(\frac{\vec{u}\cdot\vec{u}}{2}\right) - \vec{u}\times\vec{\xi} = \frac{-\nabla P}{\rho} + \frac{\nabla\cdot\tau}{\rho} + \vec{g} \tag{8.5}$$

by utilizing $\left(\vec{u}\cdot\nabla\right)\vec{u} = \nabla\left(\frac{1}{2}\vec{u}\cdot\vec{u}\right) - \vec{u}\times\vec{\xi}$. By taking the curl, Eq. (8.5) can be expressed as:

$$\begin{aligned}\frac{D\vec{\xi}}{Dt} &= -\vec{\xi}\left(\nabla\cdot\vec{u}\right) + \left(\vec{\xi}\cdot\nabla\right)\vec{u} + \frac{1}{\rho^2}\nabla_\rho\times\nabla P \\ &\quad -\frac{1}{\rho^2}\nabla_\rho\times\left(\nabla\cdot\tau\right) + \frac{1}{\rho}\nabla\times\left(\nabla\cdot\tau\right) + \nabla\times\vec{g}\end{aligned} \tag{8.6}$$

In this case, the flow is regarded as a Newtonian fluid with consistent density and viscosity. Thus, the second, fourth, fifth and seventh parts of Eq. (8.6) can be neglected. By using $\nabla \cdot \tau = \mu \nabla^2 \vec{u}$, a simplified equation is given as:

$$\frac{D\vec{\xi}}{Dt} = \left(\vec{\xi} \cdot \nabla\right)\vec{u} + \upsilon \nabla^2 \vec{\xi} \tag{8.7}$$

where υ denotes fluidic kinetic viscosity. Despite of the mathematical expression of Equation [7], there is physical diffusion phenomenon. The Lamb-Oseen vortex is a typical example. During this diffusion process, a two-dimensional axisymmetric vortex is placed in an initially inviscid and infinite fluid. Based on Eq. (8.7), a clarified equation is written in a following form:

$$\frac{\partial \vec{\xi}}{\partial t} + \left(\vec{u} \cdot \nabla\right)\vec{\xi} = \left(\vec{\xi} \cdot \nabla\right)\vec{u} + \upsilon \nabla^2 \vec{\xi} \tag{8.8}$$

The Oseen vortex is two-dimensional, which means that $\nabla \vec{u}$ is confined into a two-dimensional plane. Since $\vec{\xi}$ is perpendicular to this plane, the third term of Eq. (8.8) is considered as zero. Additionally, a radially directed $\nabla \vec{\xi}$ is orthogonal to purely tangential $\vec{u}$, which leads to a vanished second term. Therefore, Eq. (8.8) can be simplified as:

$$\frac{\partial \xi_z\left(r,t\right)}{\partial t} = \upsilon \nabla^2 \xi_z\left(r,t\right) \tag{8.9}$$

The Poisson equation can be solved with a similarity variable solution $\xi_z = f(\eta)/t$, here, $\eta = r/\sqrt{\upsilon t}$, and r denotes the separation distance from the vortex core. The approximate solution is shown as following:

$$\xi_z\left(r,t\right) = \frac{0}{4\pi\upsilon t}\exp\left(\frac{-r^2}{4\upsilon t}\right)\left(r > R\right) \tag{8.10}$$

$$u_\theta = \left(\frac{0}{2\pi r}\right)\left[1 - \exp\left(-\frac{r^2}{4\upsilon t}\right)\right]\left(r > R\right) \tag{8.11}$$

where u_θ denotes the tangential velocity distribution, R is the radius of the vortex core, and Γ_0 represents the original circulation of the vortex. The proposed model clearly illustrates the ambient flow generated by a VPNS for the following reasons: [1] because of fluid vorticity, the vorticity decays with the decreased distance to the VPNS core; [2] the inertia forces could be neglected, and the laminar Navier-Stokes equation can be applied in this model; [3] there are no axial or radial velocities generated in this model, and the rotating frequency is fixed.

Since the core of VPNS is propelled by the external magnetic field, the vorticity of the core part will not decay. Thus, hypotheses that the VPNS core performs rigid rotation, vorticity maintains an identical value in the core part, and the velocity distribution and the distance to the core part have a linear relationship are predefined. Thereby, the mathematical formula of vorticity and velocity distribution can be calculated as:

$$\xi_z = \frac{\Gamma_0}{\pi R^2}(r < R) \tag{8.12}$$

$$u_\theta = \frac{\Gamma_0 r}{2\pi R^2}(r < R) \tag{8.13}$$

The vortex can be demonstrated with the proposed model of tangential velocity and vorticity, as depicted in Fig. 8.5a, b, respectively. This model is used to analyse a VPNS with a radius of 8×10^{-4} m. The flow tangential velocity presents a linear increase and vorticity maintains constant in VPNS core ($r < 8 \times 10^{-4}$ m). However, the flow tangential velocity performs a gradual decrease, and the vorticity presents a rapid decline (approximately decrease to 1/s at 1.5 mm apart from the core centre). To straightforwardly illustrate the velocity distribution of the whole system, a schematic diagram is depicted in Fig. 8.5c. The magnitude of the flow velocity is represented by the size of the arrows. The red arrows denote the velocity distribution in the vortex core, while the blue ones represent the same parameter in the ambient

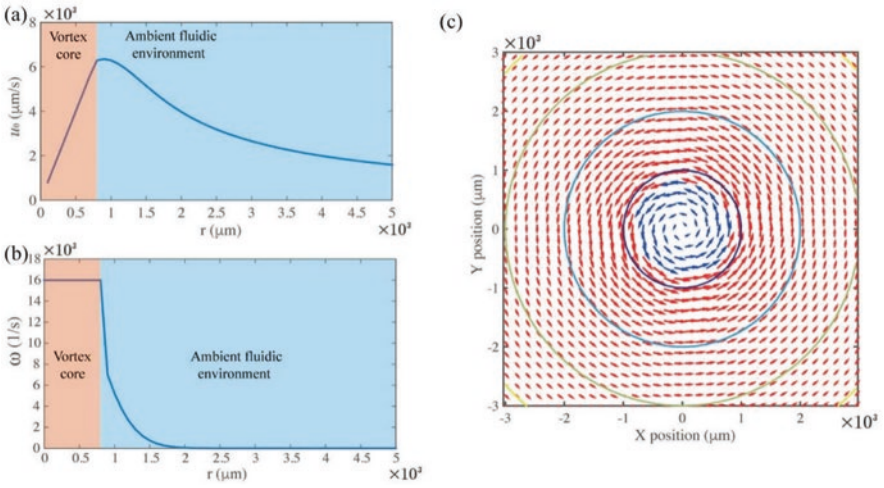

Fig. 8.5 Tangential velocity distribution (**a**) and vorticity distribution (**b**). (**c**) depicts the tangential velocity of vortex. The blue arrows denote the flow inside vortex core, while the red arrows represent that outside the core. The magnitude of flow velocity is denoted by the arrow size and the gradient of vortex vorticity is represented by coloured circles

flow. As shown in Fig. 8.5a, c, we conclude that the tangential velocity of the flow reaches the maximum value approximately at the edge of VPNS core.

8.5 Pattern Transformation of VPNS

8.5.1 Core Size Modification

It is necessary to alter the core size of VPNS if it encounters a complex fluidic environment such as there are some microchannels with various diameters. Theoretically, we know the circulation is an integration given by $\Gamma = \oint_{\mathrm{c}} \vec{u}\,\mathrm{d}l$. Thus, if we take the derivative:

$$\frac{d}{\mathrm{d}t} = \frac{\mathrm{d}}{\mathrm{d}t}\oint_{\mathrm{c}} \vec{u}\,\mathrm{d}l \tag{8.14}$$

Based on Kelvin's theorem:

$$\Gamma_{\mathrm{a}} = \Gamma + f_{\mathrm{c}} A_{\mathrm{n}} \tag{8.15}$$

where f_{c} is the Coriolis parameter and A_{n} denotes the area of the vortex. By takingthe derivative of Eq. (8.15), we can get $\frac{d\Gamma}{\mathrm{d}t} = -f_{\mathrm{c}}\frac{\mathrm{d}A_{\mathrm{n}}}{\mathrm{d}t}$. Combining previously mentioned equations, we can further obtain:

$$\frac{d}{\mathrm{d}t} 2\pi r u = -f_{\mathrm{c}}\frac{d}{\mathrm{d}t}\pi r^2 \tag{8.16}$$

According to the circulation conservation, the circulation of VPNS maintains the same value although the size is changing:

$$2\pi r u + \pi f_{\mathrm{c}} r^2 = 2\pi r_0 u_0 + \pi f_{\mathrm{c}} r_0^2 \tag{8.17}$$

where u_0 and r_0, respectively, represent the initial tangential flow velocity and the initial radius of the vortex core. Thus, the mathematical relationship between the coverage area of the pattern and the rotating frequency can be expressed by:

$$w = \frac{f_{\mathrm{c}}\left(r_0^2 - r^2\right) + 2v_0 r_0}{2r^2} \tag{8.18}$$

Notably, the experimental section will discuss the comparison and analysis between the theoretical model and experimental results.

8.5.2 Spread State

Since a VPNS is able of performing pattern swelling, they can be utilized as reconfigurable robotic end effector. As previously illustrated in Fig. 8.2, these chains perform a dynamic balance inside a stable VPNS. This is because the three major forces, namely, the magnetic repulsive forces, vortex short-range interactions which are activated by single-chain rotation and inward vortex forces induced by the major vortex, are dynamically balanced. The swarm swelling is merely confined by inward vortex forces which maintain the vortex-like pattern of the swarm. The vorticity and inward forces have an approximately linear relationship. This means that reducing vorticity will cause a decrease of inward forces, which will further cause a decrease of rotating frequency. The magnetic forces dominate the behaviour of this particle swarm when the inward forces decline, which means that the VPNS pattern is capable of swelling with high flexibility.

However, long chains will develop if we only reduce the rotating frequency of the input magnetic field f_f. This is due to the attractive interactions between head-to-tail chains. These long chains will cause predominantly modified vortices and a vanishment of vortex-like swarm. Increasing the input magnetic field f_f is one of those approaches to avoid this situation. Their rotating frequency f_{cr} declines due to the step-out behaviour of rotating chains, which will cause the change of inward vortex forces. Thereby, it is required to investigate the relationship between the input magnetic field f_f and the rotating frequency f_{cr}. This enables the estimation of swelling area of a VPNS in the spread state.

To estimate the rotating frequency of a step-out paramagnetic particle chain, a schematic demonstration is shown in Fig. 8.6. At the initial stage, the long axis of the chain coincides with the direction of the external magnetic field at position 1 (P1) depicted in Fig. 8.6a. The field and chain rotate with angular velocity ω_f and ω_c, respectively. When magnetic field rotates θ_f and reaches position 2 (P2), the direction of the chain is coincidently perpendicular to the direction of magnetic field. This leads to a 90° phase lag. When θ_l exceeds 90°, the chain performs a counterwise rotation due to the paramagnetic nature of the particles, which means that the chain rotates in a reverse direction compared with its original direction. Meanwhile, the magnetic field maintains the same direction which is clockwise (shown in Fig. 8.6b). Eventually, the chain and the magnetic field obtain coincidence again. The reverse angle of the chain is θ_b, which is depicted in Fig. 8.6c. A whole step-out cycle is demonstrated using Fig. 8.6. We predefine t_1, t_2 as the time where the phase lag changes from position 1 to position 2 and from position 2 to position 4 and θ_p as the rotating angle of the chains. Thus, they can be expanded as the following equations:

$$t_1 = \frac{\pi / 2}{2\pi \left(f_f - f_{cr} \right)} \tag{8.19}$$

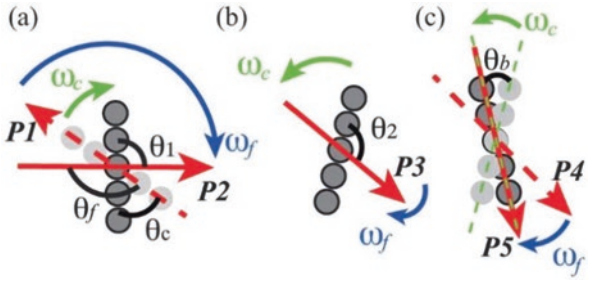

Fig. 8.6 Step-out rotating process of a paramagnetic nanoparticle chain. The green arrows indicate the angular velocity of particle chain ω_c, while the blue ones denote the rotating magnetic field ω_f. The direction of magnetic field is denoted by red dotted arrows, and the particle chain at the last moment is represented by the lighter grey particles. The chain rotates θ_c, whereas the field rotates θ_f in (**a**). In (**a**)–(**b**), θ_1 and θ_2 denote the phase lag at different moments. The chain rotates reversely with an angle θ_b, shown in (**c**)

$$t_2 = \frac{\pi / 2}{2\pi\left(f_\mathrm{f} + f_\mathrm{cr}\right)} \tag{8.20}$$

$$\theta_\mathrm{p} = \theta_\mathrm{c} - \theta_\mathrm{b} = \frac{\pi f_\mathrm{cr}^2}{f_f^2 - f_\mathrm{cr}^2} \tag{8.21}$$

$$T_0 = t_1 + t_2 = \frac{f_\mathrm{f}}{2\left(f_\mathrm{f}^2 - f_\mathrm{cr}^2\right)} \tag{8.22}$$

where $\theta_\mathrm{c} = w_\mathrm{c} t_1 = \frac{\pi f_\mathrm{cr}}{2\left(f_\mathrm{f} - f_\mathrm{cr}\right)}$, $\theta_\mathrm{b} = w_\mathrm{c} t_2 = \frac{\pi f_\mathrm{cr}}{2\left(f_\mathrm{f} + f_\mathrm{cr}\right)}$, $f_\mathrm{cr} = \frac{\omega_\mathrm{c}}{2\pi}$ represents the rotating frequency of chain, and $f_\mathrm{f} = \frac{\omega_\mathrm{f}}{2\pi}$ denotes the rotating frequency of the field. Since there are $N = \frac{2\pi}{\theta_\mathrm{p}}$ cycles in a round (2π). Therefore, the average frequency of a step-out chain is shown as follows:

$$f_\mathrm{r} = \frac{1}{NT_0} = \frac{f_\mathrm{cr}^2}{f_\mathrm{f}} \tag{8.23}$$

To obtain the relationship between input rotating frequency and the inward vortex forces, it is necessary to make the following assumptions: [1] the inward vortex forces are proportional to the rotating frequency of the vortex f_v; [2] the vortex and the input rotating frequency have a linear relationship.

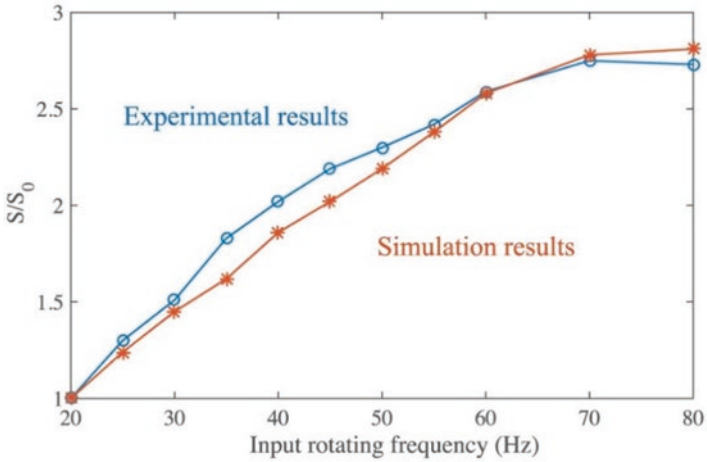

Fig. 8.7 Experimental and simulation results of changing ratio of pattern area in spread state. The area when input rotating frequency is 20 Hz is represented by S_0

We use COMSOL to conduct the simulation during which the short chains are considered as single particles. At the beginning, magnetic repulsive forces will be exerted between the particles. Meanwhile, the pattern will swell because the high input rotating frequencies cause the decline of inward vortex forces. Therefore, we can estimate the change of inward vortex force by combining Eq. (8.23) and the proposed hypotheses. When the chain rotates at their step-out frequencies (20 Hz), it reaches the maximum inward vortex force. During the simulation, we apply an inward vortex force to balance the magnetic repulsive forces when the input rotating frequency is 20 Hz. The reason on applying this inward force is to maintain the particles confined in the original regions. Consequently, we can estimate the maximum inward vortex forces. Additionally, they can also be estimated utilizing the changing ratio of the applied rotating frequencies since they are proportional to the rotating frequency of VPNS. Figure 8.7 shows the results of changing regions with different inward forces applied. These forces can be regarded as the inward vortex forces. Practically, the input rotating frequency f_f is not identical to the rotating frequency f_v of a VPNS and, mostly, $f_f > f_v$. Therefore, these two values should be calibrated rather than directly applying the input rotating frequency f_f. Section 5.3 will introduce the calibration approaches. Both curves of simulation and experimental results climb with the increase of input rotating frequency after this calibration. Before the input frequency reaches 70 Hz, the curve of simulation presents a linear increase. It levels out after the frequency reaches 70 Hz. Similarly, the curve of experimental results performs a climb when the frequency is low (20–45 Hz), and it gradually maintains the approximately same value when the frequency presents a continuous increase. Both simulation results and experimental results reach a value of 2.7 when the frequency reaches 80 Hz. Table 8.2 shows the core parameter which is applied in the simulation process, such as magnetic susceptibility χ_p, permeability μ_0, the volume of the particles V_p and the magnetic field strength B.

Table 8.2 Key parameters used in the simulation to estimate the swelling pattern areas in spread state

Parameter	Value
λ_p	0.8
Original area of VPNS	3.6×10^{-7} mm^2
μ_0	1.257×10^{-6} V·s/(A·m)
B	10^{-3} T
V_p	2.12×10^{-14} m^3

8.6 Experimental Results and Discussion

8.6.1 Generating a Vortex-Like Swarm

Figure 8.8 illustrates a generation process of a VPNS, where the nanoparticles are initially dispersed in the empty workspace. Then, we apply a rotating magnetic field. Firstly, it can be observed that the particle chain performs a self-rotation and next a highly concentrated region of particles is generated. Finally, a VPNS with dynamic equilibrium forms. We can also observe a self-rotation of particle chain in the peripheral area of the particle swarm. Meanwhile, they rotate around the vortex centre with the approximately equal radius. This is because the radial components of the interaction forces are dynamically balanced. When time t reaches 80s, the majority of particle chains aggregate into the vortex core, as shown in Fig. 8.8. However, some chains fail to be attracted due to the fluidic influence. Moreover, these particle chains are not attracted as a solid entity inside the cortex core. During the centripetal attraction process, some can be successfully attracted into the core, while the others are ejected because of centrifugal forces. To conclude, the vortex is a dynamically balanced system, which closely matches the theories discussed in Sect. 2.

Region I of Fig. 8.8 shows that the nanoparticles induce vortices using weak fluidic interactions at low rotating frequency (e.g. 2 Hz). This means that the nanoparticle can only perform chain-like structure. However, the coverage area does not shrink which is shown in the inset (6 mT, 2 Hz). The fluidic inward forces steadily increase when the frequencies reach 3 Hz. Region II (blue square) in Fig. 8.8 well illustrates this stage. The particle chains tend to aggregate into a smaller area with approximately 40% of them ejected. Simultaneously, the swarm is unstable due to their loose aggregation inside the VPNS, which is discussed previously. The VPNS forms in the region III, in which most particle chains are successfully aggregated. Lower strengths (4 mT) of magnetic field lead to a narrow range (3.5–5 Hz) of rotating frequency, while larger strengths (10 mT) can enlarge the range (4–10 Hz) of rotating frequency. When the strengths are higher than the upper red dotted line (region IV), the VPNS forms with much more loss again. This is because the fluidic forces are not capable of aggregating the majority of nanoparticle chains, which cause a smaller core. In region V, the nanoparticles tend to form multiple vortex-like swarms with a continuous increase of rotating frequency. This is because there is no dominating vortex that forms with the fluidic forces and chain lengths decrease. Consequently, some multiple vortices with much smaller size form.

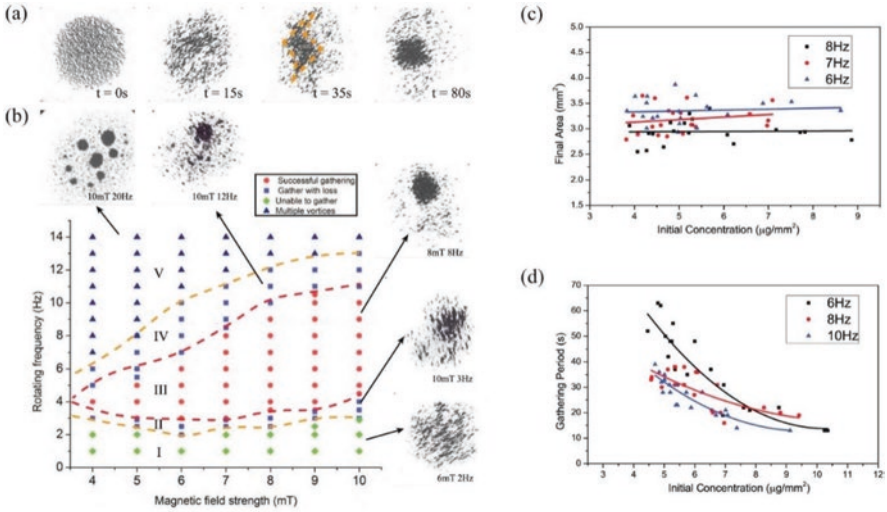

Fig. 8.8 (**a**) The generation process of a VPNS. (**b**) A successful formation of a dynamically balanced VPNS. It presents four different states of swarm, namely, successful aggregation, aggregation with loss, failure to aggregate and multiple vortices formation, shown in different icons. The red and yellow dotted curves are highlighted as boundaries of these four states. The figure insets show the experimental results. (**c**) The relationship between the initial concentrations and the final areas under the rotating fields with frequencies of 6, 7 and 8 Hz. The strength of magnetic field is valued as 8 mT and the data points fit the lines. (**d**) The aggregation periods with different initial concentrations and input rotating frequencies

8.6.2 Characterization of a VPNS

We conduct the aggregation process in region III in which the nanoparticles are successfully aggregated with different initial concentrations of particles and rotating frequencies to evaluate the effectiveness of this proposed approach. In fact, the same amount of particles and the same fixed initial conditions such as rotating frequencies, field strength and total amount of particles will lead to the same final areas of the patterns. Thus, different initial concentrations of nanoparticles cause different final areas of pattern, as illustrated in Fig. 8.8c. However, the curves maintain constant with the increase of initial particle concentration. The increasing rate of these curves is lower than 10%. The small increasing rate demonstrates that the final areas are weakly coupled with the initial concentrations, which shows the high efficiency of this method in aggregating dispersed paramagnetic nanoparticles. A lower initial concentration of particles leads to a larger initial coverage area if the amount of particles is equal. Since the fluidic forces are too low to successfully aggregate the particles in the peripheral region, the curves increase slightly.

As shown in Fig. 8.8c, the maximum rotating frequency 8 Hz leads to the minimum pattern, while the minimum rotating frequency 6 Hz leads to maximum final area. Circulation conservation which is expressed in Eq. (8.15) is a good

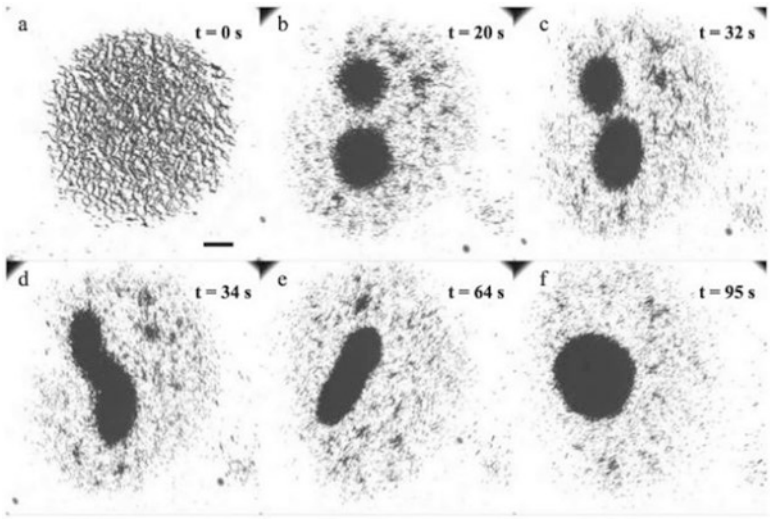

Fig. 8.9 Self-merging process of two individual VPNSs. The magnetic field strength is 7.5 mT, the rotating frequency is 8 Hz, and the scale bar is 500 μm

explanation of these results. Figure 8.8d shows the aggregation periods of the vortex-like swarm with different initial nanoparticle concentration. A higher initial particle concentration causes shorter average distance between particle chains. This also leads to the decrease of aggregation periods with initial particle concentration among the whole particle concentration range. Thus, it takes less time to attract particle chains towards each other before the merging process. The curves will gradually keep the equal value with initial concentration increases. Unfortunately, the results present some uncertainties due to the random assembly process. The uncertainties include different amounts of particle loss and measurement error of coverage areas. To statistically depict the principles of particle aggregation process, we use scatter diagrams and linear fitting. The self-merging process of two independent VPNSs is conducted to validate the simulation results. Figure 8.9 shows the experimental results. In the initial stage, a magnetic field which is located in region V (Fig. 8.8a) is applied and particles have a low suspended concentration (5 μg/mm^2). Two self-governed VPNSs have been generated during the experiments. The relative distance between the two VPNSs can reach the critical value $(a/d)_c$, illustrated in Fig. 8.8b. The distance of them will decrease gradually. The attractive fluidic interactions cause the deformation of them before they start to contact with each other. This is demonstrated in Fig. 8.8c. Figure 8.8d, e illustrates the merging process of the two swarms when they begin to contact. The merged swarm presents a prolate shape. The difference between long axis and short axis of the swarm performs a gradual decrease. An axisymmetric circular VPNS is finally generated. This means the simulation results closely match the experimental results.

8.6.3 Pattern Transformation of a VPNS

Change of Core Size

Using the blue curve in Fig. 8.10, the change of pattern area has been demonstrated. The final pattern area of swarm decreases with the rotating frequency increasing from 5 to 10 Hz. We use red circles to label the experimental results. The differences between the experimental data and the model are slightly low (approximately 5%) at lower rotating frequency (< 6 Hz). However, they reach more than 20% if the input rotating frequency is larger than 7 Hz. The inconsistency of rotating frequency causes this phenomenon. We assume that the frequency of rotating vortex f_v and the input frequency f_f are identically valued with a constant $f_\alpha$in the mathematical model. To induce a vortex with a frequency of $f_v = f_\alpha$, the input frequency of magnetic field should be larger than the threshold f_α. Thus, the experimental rotating frequency should be higher than those of the model for any changing ratio of pattern area.

The original mathematical equation is required to be modified if we demand a better estimation for changing ratio. It is difficult to attain the analytical model since the difference between the frequency of rotating vortex f_v and the input frequency f_f is the main error. Thus, it is calibrated using experimental data shown in Fig. 8.11. The reflection between two frequencies is given by the linear fitting lines. The model is modified by unifying two frequencies (f_v and f_f) based on the previous relationship. It is also illustrated using yellow curves in Fig. 8.11. The changing ratio can be estimated using this modified model with a higher performance among all frequency ranges.

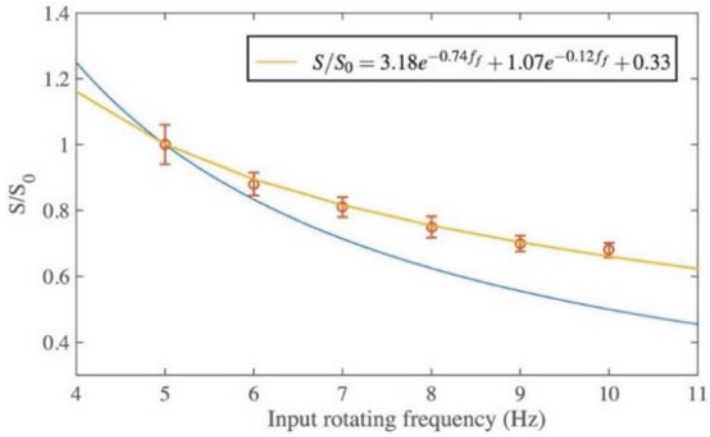

Fig. 8.10 The relationship between the pattern area and the input rotating frequency. The blue curve indicates the original model, and the yellow curve denotes the modified model. The red circles represent the experimental data. S_0 denotes the coverage area at rotating frequency of 5 Hz

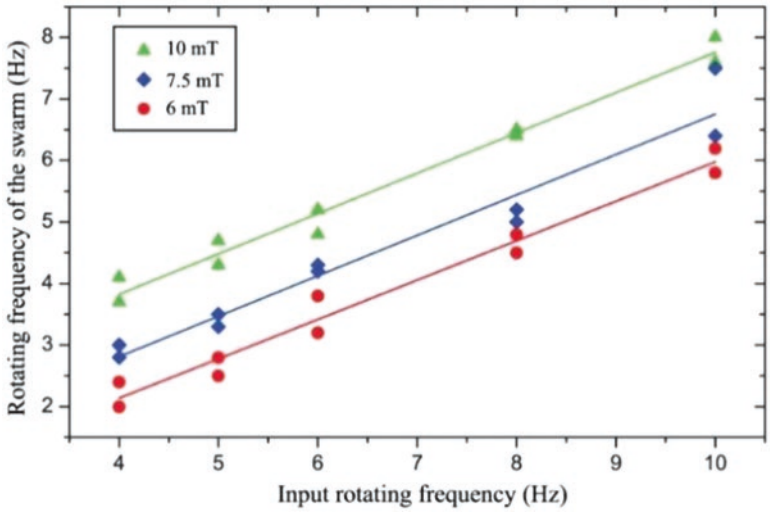

Fig. 8.11 Calibrated results between the input frequency and the rotating frequency of a VPNS. The relationship of them under field strength of 10 mT, 7.5 mT and 6 mT is denoted by green, blue and red lines

Spread State of VPNS

The pattern area is strongly relevant to the input frequency of magnetic field if a stable VPNS is generated. Figure 8.12 depicts the results in the frequency range of 0–90 Hz. Initially, the paramagnetic particles are dispersed and a VPNS is generated gradually. We predefine the original coverage area as S_0 and we choose 5 Hz as the original rotating frequency. With the increase of rotating frequency, the pattern area shrinks to $0.65S_0$. Then, the VPNS encounter a stable period with the rotating frequency ranging from 10 to 20 Hz. During this period, the pattern area keeps approximately same size. A VPNS with a high particle concentration forms within this frequency range, which is illustrated in the corresponding inset in Fig. 8.12. Interestingly, the VPNS performs a spread state when the rotating frequency exceeds 20 Hz (from 20 to 70 Hz). It swells three times larger than its initial area (from $0.65S_0$ to $1.85S_0$). A spindle-like pattern forms which is shown in the Fig. 8.12 inset. The frequency range where an effective VPNS can be generated with a stable contour and dynamically balanced characteristics is shown in Fig. 8.13 using red region. The step-out behaviour of particle chain causes a significant decrease of inward vortex forces during this spread state. Thus, we can observe some vital features of a dynamically balanced VPNS in this state. For example, few nanoparticle chains rotate around the vortex centre, the swarm contour is unstable, and it is difficult to remain the vortex-like structure during locomotion.

In fact, during the spread state, a high input frequency can propel a VPNS to enter the spread state, and reversely, the particle swarm can reform an effective VPNS once the input frequency is lower than 20 Hz. This reversed state is shown in

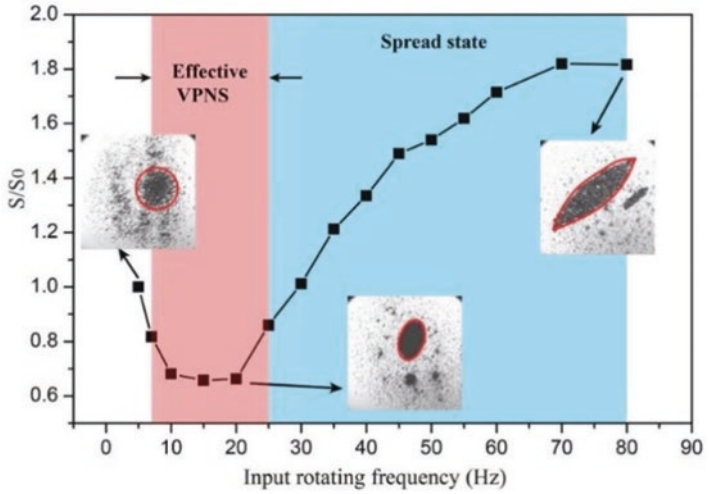

Fig. 8.12 The relationship between the pattern area and the input frequency. The red region represents a dynamically balanced VPNS which is assembled by paramagnetic nanoparticles with a stable contour. The spread state is denoted by the blue region. Three insets show the pattern area when the input rotating frequency is 5, 20 and 80 Hz with a field strength of 7.5 mT

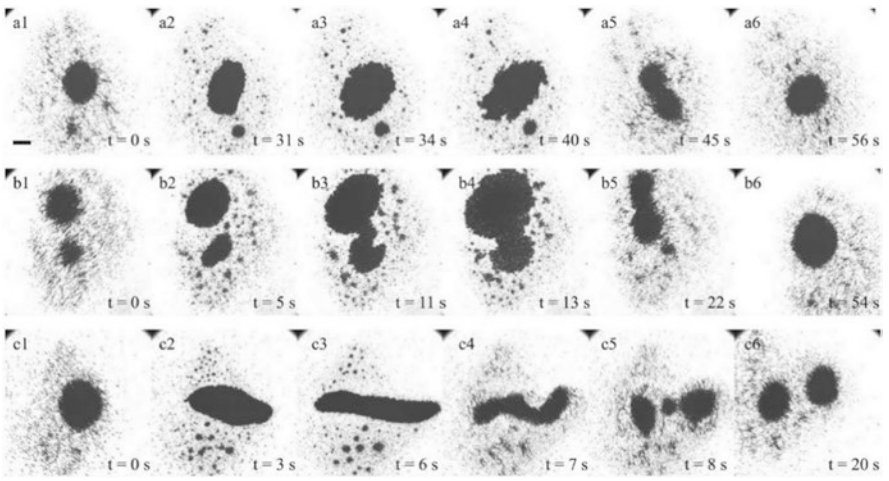

Fig. 8.13 Experimental results. (*a1*)–(*a6*) show the reversible state, (*b1*)–(*b6*) denote the merging process of two VPNSs, and (*c1*)–(*c6*) represent the splitting process of a merged VPNS. The field strength is 7.5 mT and the scale bar is 600 μm

Fig. 8.13a1–a6. We apply a rotating magnetic field with 8 Hz frequency to generate a VPNS, which is demonstrated in Fig. 8.13a1. The rotating frequency increases to 25 Hz at t = 30 s, which can trigger the spread state. Figure 8.13a2 shows that the VPNS pattern presents an immediate swelling after triggering. The swarm contour

becomes extremely unstable and shows a gear-like pattern when the input frequency continuously increases to 40 Hz at $t = 32$ s. This phenomenon is shown in Fig. 8.13a3, a4. At the final stage, the VPNS recovers the original state and presents a stable circular structure.

The parameter of the actuating rotating magnetic field locates in region V in Fig. 8.8 in the aggregation process, which leads to the generation of multiple vortex-like swarms. Motion control and path planning can be easily implemented if those vortex-like swarms can be merged into one dominating swarm. Figure 8.13b1–b6 shows this merging process. We apply a 12 Hz input rotating frequency, and the originally dispersed particles are transferred to two VPNSs. The condition of critical value $(a/d)_c$ is not reached since the self-merging phenomenon cannot remain more than 60 s. Therefore, we require a new strategy to merge the multiple vortices during the simulation. The input frequency reaches 40 Hz, and the pattern swells significantly at $t = 2$ s. Afterwards, the critical situation of the merging process during which two swarms start to contact with each other appears, which is demonstrated in Fig. 8.13b3, b4. The merging process completes after the input frequency declines to 6 Hz, illustrated in Fig. 8.13b5, b6.

As stated previously, the merging process is reversible. Figure 8.13c1–c6 demonstrates the reversely splitting process of merging. During this process, a dominating VPNS is split into two individual nanoparticle swarms with smaller size. To trigger the spread state, we apply an elliptically rotating magnetic field with an 80 Hz frequency. The strength along the short axis is three times higher than the strength along the long axis. This field can also enlarge the pattern area. Figure 8.13c2, c3 depicts the generation of a strip-shaped pattern. With the field frequency decreasing to 12 Hz, a circular rotating field forms again after $t = 6$ s. Figure 8.13c4 shows the distortion of the pattern. In fact, the spread state presents a shorter period if the recover frequency is low (8 Hz). This causes that the pattern will not be distorted and start to rotate around its centre. By applying a larger recover frequency, we can observe the splitting process. During this process, the particle chains shorten, and the influence range of vortex force is smaller. As illustrated in Fig. 8.13c5, c6, the swarm in different regions tends to aggregate locally. Finally, two VPNSs form.

8.6.4 Morphology of Swarm Pattern During Locomotion

Motion in a Synchronized Fashion

When an object starts to contact a wall, the drag coefficient increases. This causes unbalanced fluidic interaction forces which are exerted on different regions of this object. Therefore, the motion velocity of the main part of the object is larger than those of the other parts. By increasing the pitch angle of the input rotating frequency, the two-dimensional locomotion can be realized. Notably, the velocity of a moving VPNS and its morphology are significantly determined by the pitch angle,

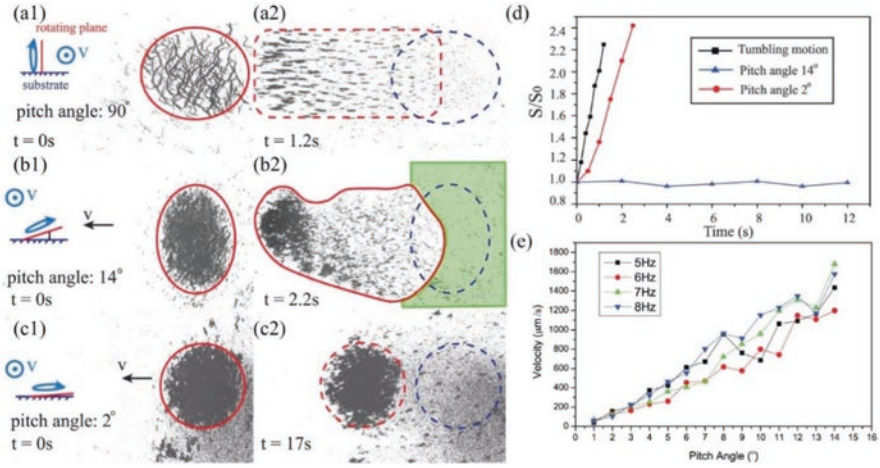

Fig. 8.14 Changes of swarm pattern morphology during the locomotion. The red circles in (**a1**), (**b1**) and (**c1**) show the original swarm shape, while the red dotted circles in (**a2**), (**b2**) and (**c2**) denote the final areas. The blue dotted circles in (**a2**), (**b2**) and (**c2**) show the original locations of the swarm. Spread particles in the green region are not initially located in the swarm; thus the region is not included into the area of the swarm. Schematic illustrations in (**a1**), (**b1**) and (**c1**) demonstrate the relationship between the direction of the applied magnetic field and the direction of the translational locomotion of the swarm. The VPNS moves perpendicular to the inclination direction of the magnetic field. The areal change in different motion modes with time is shown in (**d**), and the moving velocity of a VPNS with different pitch angles is shown in (**e**)

which is depicted in Fig. 8.14. The nanoparticle chains fail to form in an in-plane fluidic vortex if the value of pitch angle is 90°. The paramagnetic nanoparticle chain will attract each other head-to-tail in the tumbling motion. Thereby, there are many chains with different lengths. This causes different moving velocities of chains. Figure 8.14a1, a2 demonstrates an enlarged swarm pattern. The VPNS pattern cannot be remained and the vortex steadily decays if the value of pitch angle decreased to 14°. This is shown in Fig. 8.14b1, b2. If the pitch angle further decreases to 10°, the VPNS recovers its original morphology and a dynamic equilibrium can be remained in motion. As demonstrated in Fig. 8.14c1, c2, the majority of particle chains are confined inside the vortex core and move with a synchronized fashion when the value of pitch angle is lower than 2°. Figure 8.14b shows the changing ratios of the coverage area of swarm pattern. These ratios are propelled by rotating frequency with different values of pitch angle: 90°, 14° and 2°. The coverage area which can make tumbling motion presents a significant swelling over 90% in 1 s with a constant increasing rate. The coverage area performs a slow increase in 0.5 s and presents an equal increasing rate which is discussed before when the pitch angle is 14°. The dynamically balanced state cannot be remained since the vortical shape is unstable. Thus, this causes irregular fluidic interaction forces and a large loss of nanoparticles which is simultaneously out of control. The changing range of coverage area is less than 5% which explains a stable VPNS during the motion.

By controlling the morphology of VPNS, the delivery of nanoparticles can be realized synchronously. Next section will well demonstrate the critical input parameters. Using a larger pitch angle to actuate a swarm can lead to an elongated pattern and a higher translational velocity. However, this enlarged pattern will cause a low access rate and precision. Thus, it is necessary to actuate a particle swarm as a VPNS because the pattern is under control in the motion. Additionally, it can generate a higher access rate for a targeted delivery.

Figure 8.14e shows the velocities of a mobile VPNS. We have applied a rotating field with different frequencies and pitch angles to propel the VPNS. The translational velocities perform a linearly increasing relationship with its pitch angle. As shown in Fig. 8.14e, we can conclude that the translational velocity and the rotating frequency are loosely coupled. This is because a higher frequency splits chains into shorter chains, which make a constant translational velocity. Although the increased rotating frequency can make a faster velocity, the split chains dominate predominantly.

Tuneable Trapping Forces of VPNSs

The majority of particles will be constrained inside the core of VPNS since they are restricted by the fluidic trapping forces generated by VPNS. Therefore, the movement of the swarm can be considered as the motion of entire swarm. Moreover, it is required to investigate the fluidic trapping forces, because they affect the input parameters which influence the morphology of the swarm during locomotion. Multiple polystyrene marker microparticles are introduced to illustrate the tuneable trapping forces of VPNSs. Figure 8.15 shows the results. As shown in Fig. 8.15a1, b1, c1 and d1, the propelled VPNSs approach and trap the polystyrene marker microparticles which are randomly distributed. Due to the fluidic interaction, the VPNS will attract the microparticles. Figure 8.15a2, b2, c2 and d2 shows that the microparticles are trapped into the VPNSs' core. The parameters of propelling magnetic field used to collect microparticles in four cases are equal: the field strength is 6 Hz, the rotating frequency is 8 Hz, and the pitch angle is 5°. Figure 8.15a1–a3 demonstrates a successful trapping and transporting of multiple microparticles. The parameters of magnetic field in the transportation process are equal to those parameter during the collecting process. Since the VPNS maintains stable state, all cargos are successfully trapped by the VPNS during the motion. Then the input rotating frequency is decreased to 4 Hz and the other parameters remain having the same value. Figure 8.15b3 indicates that the inward vortex forces is reduced. This is because two microparticles leak from the core while three microparticles are initially trapped into the core. Increasing rotating frequency can enhance the inward trapping forces based on the comparisons of Fig. 8.15a1–a3 and b1–b3.

To increase the motion velocity of VPNS, the pitch angle is increased to 5°. Meanwhile, the field strength and rotating frequency remain the equal value in the case of Fig. 8.15a2, a3. However, it is incapable to trap all microparticles. Two microparticles eject from the core of vortex, which is depicted in Fig. 8.15c3. Comparing

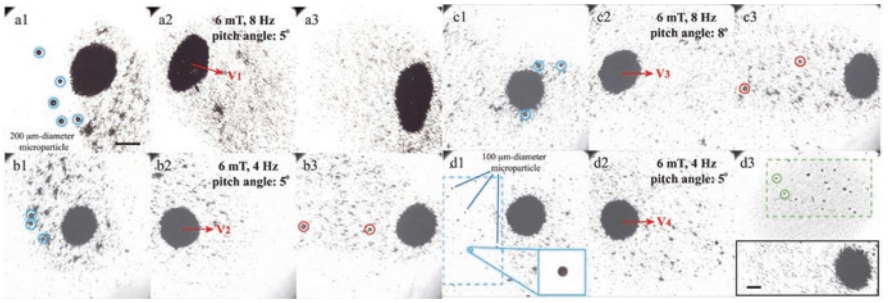

Fig. 8.15 Investigating the behaviours of non-magnetic marker microparticles under different conditions of magnetic fields with experiments to validate the trapping forces of VPNSs. The blue circles show the randomly distributed microparticles, red circles denote the leaking microparticles from the VPNS core, and the green circles are the trapped microparticles by the VPNS. The red arrows represent the velocity of VPNSs. The scale bar is 800 μm and the scale bar of the inset is 500 μm

Fig. 8.15c1–c3 with a1–a3, the trapping capability of the VPNS is affected by the motion velocity of the background flow, and the stability of the vortical structure is weakened by a high velocity of the flow.

Furthermore, Fig. 8.15d1–d3 shows that microparticles with different inertia are applied. All the parameters of input magnetic field are equal to those parameters in the case of Fig. 8.15b3–b4 after collecting all smaller microparticles. As a result, the mobile velocity of VPNSs is equal ($V_4 = V_2$). Figure 8.15d3 illustrates that no microparticles eject from the core of VPNS. It is difficult to identify these small microparticles since nanoparticle swarm exists. It is necessary to apply a uniform magnetic field which is perpendicular to the experimental plane if we require an improvement of observation, shown in Fig. 8.15d3. The microparticles still remain inside the swarm. The microparticles with smaller inertial coefficients have a higher tendency to be trapped by the same VPNS by analysing Fig. 8.15d1–d3 and b1–b3. The experimental results closely match the results presented by mathematically analytical model and simulation. Therefore, the synchronized locomotion of VPNS can be ensured by higher input frequencies, smaller moving velocities and nanoscale of building blocks of the nanoparticle swarm.

Locomotion in a Channel

The VPNS can easily penetrate through a branched channel because of the morphology stability of a mobile VPNS. This process is illustrated in Fig. 8.16. A VPNS navigates from the left reservoir to the target one. As demonstrated in Fig. 8.16a1, it first locates at the entrance of a semicircle-shaped channel with two branches. Then, Fig. 8.16a2–a5 shows that it penetrates through the channel. The green spots in Fig. 8.16b1–b5 show the real-time locations of the VPNS in the channel. Furthermore, it is required for a VPNS to penetrate through an angled channel,

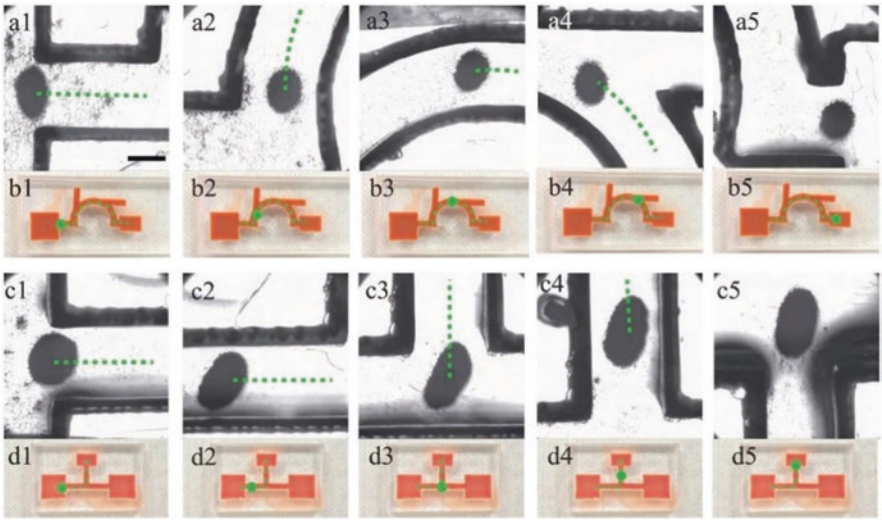

Fig. 8.16 Illustrations of propelling swarms to penetrate through two different microchannels. The VPNSs in semicircle-shaped and angled channels are shown by (*a1*)–(*a5*) and (*c1*)–(*c5*), respectively. (*b1*)–(*b5*) and (*d1*)–(*d2*) indicate an overall view of the semicircle-shaped and angled branched channels. The corresponding real-time locations of swarms are represented by green spots with an 800 μm scale bar

which is shown in Fig. 8.16c1–c5, and Fig. 8.16d1–d5 shows the channel. According to the figures proposed, the majority of nanoparticles can successfully reach the targeted reservoir although there are few fragments left inside the channel. An image processing application is utilized to compute the access rate of VPNS. We compare the areas of particle clusters reaching the target and those left inside the channel. Consequently, the particle swarm which can be regarded as a vortex-like entity has an extremely high accessing rate. It can, respectively, reach 91.6% and 96.8% for different cases in the semi-circular and angled channels.

We apply tumbling magnetic fields to propel the nanoparticle chains, during which the swarms elongate remarkably. The branches of channels cause extremely low access rate. Thus, few particles can reach target reservoir. Moreover, the access rate is lower than 10% in semi-circular channels, while it reaches 50% in the angled channel. These results show that the generation of dynamically balanced vortex-like swarm can ensure a high accuracy and precision of drug delivery for the target delivery applications.

Discussion on Imaging Modality

The proposed model can be used for imaging applications. Clinical MRI systems have following advantages, such as visualization of soft tissues and reduction of ionizing radiation exposure. In vivo particle tracking can be implemented due to its

high resolution. However, it also presents some drawbacks. For example, the rotation and translation of the particle swarm will be obstructed by its strong magnetic field. Thus, performing imaging of the motion is difficult. Practically, integration of additional coils is necessary to generate a rotating field with a constant field strength. Similarly, X-ray imaging can also cause some challenges for tracking VPNSs in vivo. The electromagnetic coils should be placed between the X-ray generator and receiver. However, the magnetic field will cause the distortion of the coils, which deteriorates the performance of X-ray imaging [47]. Moreover, although X-ray imaging can guarantee a milli-scale resolution, the long-time radiation exposure may be detrimental to patients. Hence, ultrasound imaging is regarded as an alternative approach for in vivo imaging. Ultrasound imaging uses two-dimensional ultrasound feedback to track the trajectory of objects by planning and steering the path to avoid dynamic obstacles [48]. Its resolution can reach 1–2 mm. It also has some merits such as low cost and avoidance of ionizing radiation. The approach for generating VPNS may be used to improve the imaging performance of ultrasound imaging. This is because the swarm size is capable to reach the tracking limitation by enlarging the amount of particles or applying particles with larger size.

8.7 Conclusion

This paper has discussed pattern generation, reversible merging, VPNSs splitting and navigated locomotion. The particles in VPNS chains make the swarm move as a dynamic entity because they perform synchronized motions. The models of generation process, the responses of the VPNS to the input frequency of the rotating magnetic fields and the spread state are independently illustrated. Notably, the corresponding experimental results closely match the models. The change of VPNS patterns such as the reversible merging process has been demonstrated. They can be flexibly controlled by applying magnetic field. Moreover, if the magnetic field has a small pitch angle, a VPNS can be actuated as a dynamic entity with a stable pattern. The trapping forces are illustrated with analysis and simulation of non-magnetic spheres' behaviour. It will critically affect the synchronized locomotion of the particle swarm. Finally, this paper demonstrates the penetration of VPNSs through the different channels with high accessing rates. The exploration of VPNS enables a fundamental investigation of microrobotic swarm behaviours. It can also be used for in vivo targeted drug delivery.

References

1. Nelson, B. J., Kaliakatsos, I. K., & Abbott, J. J. (2010). Microrobots for minimally invasive medicine. *Annual Review of Biomedical Engineering, 12*, 55–85.
2. Sitti, M., Ceylan, H., Hu, W., Giltinan, J., Turan, M., Yim, S., & Diller, E. (2015). Biomedical applications of untethered mobile milli/microrobots. *Proceedings of the IEEE, 103*(2), 205–224.

3. Zhang, L., Abbott, J. J., Dong, L., Kratochvil, B. E., Bell, D., & Nelson, B. J. (2009). Artificial bacterial flagella: Fabrication and magnetic control. *Applied Physics Letters, 94*(6), 064107.
4. Peyer, K. E., Zhang, L., Kratochvil, B. E., & Nelson, B. J. (2010, May). Non-ideal swimming of artificial bacterial flagella near a surface. In *2010 IEEE international conference on robotics and automation* (pp. 96–101). IEEE.
5. Zhang, L., Abbott, J. J., Dong, L., Peyer, K. E., Kratochvil, B. E., Zhang, H., Bergeles, C., & Nelson, B. J. (2009). Characterizing the swimming properties of artificial bacterial flagella. *Nano Letters, 9*(10), 3663–3667.
6. Petit, T., Zhang, L., Peyer, K. E., Kratochvil, B. E., & Nelson, B. J. (2012). Selective trapping and manipulation of microscale objects using mobile microvortices. *Nano Letters, 12*(1), 156–160.
7. Folio, D., & Ferreira, A. (2017). Two-dimensional robust magnetic resonance navigation of a ferromagnetic microrobot using pareto optimality. *IEEE Transactions on Robotics, 33*(3), 583–593.
8. Sadelli, L., Fruchard, M., & Ferreira, A. (2016). 2D observer-based control of a vascular microrobot. *IEEE Transactions on Automatic Control, 62*(5), 2194–2206.
9. De Lanauze, D., Felfoul, O., Turcot, J. P., Mohammadi, M., & Martel, S. (2014). Three-dimensional remote aggregation and steering of magnetotactic bacteria microrobots for drug delivery applications. *The International Journal of Robotics Research, 33*(3), 359–374.
10. Snezhko, A., & Aranson, I. S. (2011). Magnetic manipulation of self-assembled colloidal asters. *Nature Materials, 10*(9), 698–703.
11. Servant, A., Qiu, F., Mazza, M., Kostarelos, K., & Nelson, B. J. (2015). Controlled in vivo swimming of a swarm of bacteria-like microrobotic flagella. *Advanced Materials, 27*(19), 2981–2988.
12. Li, J., de Ávila, B. E. F., Gao, W., Zhang, L., & Wang, J. (2017). Micro/nanorobots for biomedicine: Delivery, surgery, sensing, and detoxification. *Science Robotics, 2*(4), eaam6431.
13. Becker, A., Onyuksel, C., Bretl, T., & McLurkin, J. (2014). Controlling many differential-drive robots with uniform control inputs. *The International Journal of Robotics Research, 33*(13), 1626–1644.
14. Donald, B. R., Levey, C. G., Paprotny, I., & Rus, D. (2013). Planning and control for microassembly of structures composed of stress-engineered MEMS microrobots. *The International Journal of Robotics Research, 32*(2), 218–246.
15. Martel, S., & Mohammadi, M. (2010, May). Using a swarm of self-propelled natural microrobots in the form of flagellated bacteria to perform complex micro-assembly tasks. In *2010 IEEE international conference on robotics and automation* (pp. 500–505). IEEE.
16. Vach, P. J., Walker, D., Fischer, P., Fratzl, P., & Faivre, D. (2017). Pattern formation and collective effects in populations of magnetic microswimmers. *Journal of Physics D: Applied Physics, 50*(11), 11LT03.
17. Chen, Q., Bae, S. C., & Granick, S. (2011). Directed self-assembly of a colloidal kagome lattice. *Nature, 469*(7330), 381–384.
18. Mao, X., Chen, Q., & Granick, S. (2013). Entropy favours open colloidal lattices. *Nature Materials, 12*(3), 217–222.
19. Yan, J., Bloom, M., Bae, S. C., Luijten, E., & Granick, S. (2012). Linking synchronization to self-assembly using magnetic Janus colloids. *Nature, 491*(7425), 578–581.
20. Yan, J., Chaudhary, K., Bae, S. C., Lewis, J. A., & Granick, S. (2013). Colloidal ribbons and rings from Janus magnetic rods. *Nature Communications, 4*(1), 1–9.
21. Hong, Y., Diaz, M., Córdova-Figueroa, U. M., & Sen, A. (2010). Light-driven titanium-dioxide-based reversible microfireworks and micromotor/micropump systems. *Advanced Functional Materials, 20*(10), 1568–1576.
22. Palacci, J., Sacanna, S., Steinberg, A. P., Pine, D. J., & Chaikin, P. M. (2013). Living crystals of light-activated colloidal surfers. *Science, 339*(6122), 936–940.
23. Xu, T., Soto, F., Gao, W., Dong, R., Garcia-Gradilla, V., Magaña, E., Zhang, X., & Wang, J. (2015). Reversible swarming and separation of self-propelled chemically powered nanomotors under acoustic fields. *Journal of the American Chemical Society, 137*(6), 2163–2166.

24. Diller, E., Pawashe, C., Floyd, S., & Sitti, M. (2011). Assembly and disassembly of magnetic mobile micro-robots towards deterministic 2-D reconfigurable micro-systems. *The International Journal of Robotics Research, 30*(14), 1667–1680.
25. Miyashita, S., Diller, E., & Sitti, M. (2013). Two-dimensional magnetic micro-module reconfigurations based on inter-modular interactions. *The International Journal of Robotics Research, 32*(5), 591–613.
26. Kagan, D., Balasubramanian, S., & Wang, J. (2011). Chemically triggered swarming of gold microparticles. *Angewandte Chemie, 123*(2), 523–526.
27. Snezhko, A., Belkin, M., Aranson, I.S. & Kwok, W.K. (2009). Self-assembled magnetic surface swimmers. *Physical Review Letters, 102*(11), 118103.
28. Yu, J., Wang, B., Du, X., Wang, Q. & Zhang, L. (2018). Ultra-extensible ribbon-like magnetic microswarm. *Nature Communications, 9*(1), 1–9.
29. Yu, J., Jin, D., Chan, K.F., Wang, Q., Yuan, K. & Zhang, L. (2019). Active generation and magnetic actuation of microrobotic swarms in bio-fluids. *Nature Communications, 10*(1), 1–12.
30. Yu, J., Yang, L., & Zhang, L. (2018). Pattern generation and motion control of a vortex-like paramagnetic nanoparticle swarm. *The International Journal of Robotics Research, 37*(8), 912–930.
31. Chaluvadi, B., Stewart, K.M., Sperry, A.J., Fu, H.C. & Abbott, J.J. (2020). Kinematic model of a magnetic-microrobot swarm in a rotating magnetic dipole field. *IEEE Robotics and Automation Letters, 5*(2), 2419–2426.
32. Felfoul, O., Mohammadi, M., Taherkhani, S., De Lanauze, D., Xu, Y.Z., Loghin, D., Essa, S., Jancik, S., Houle, D., Lafleur, M. & Gaboury, L. (2016). Magneto-aerotactic bacteria deliver drug-containing nanoliposomes to tumour hypoxic regions. *Nature Nanotechnology, 11*(11), 941–947.
33. Wang, B., Chan, K.F., Yu, J., Wang, Q., Yang, L., Chiu, P.W.Y. & Zhang, L. (2018). Reconfigurable swarms of ferromagnetic colloids for enhanced local hyperthermia. *Advanced Functional Materials, 28*(25), 1705701.
34. Dong, X., & Sitti, M. (2020). Controlling two-dimensional collective formation and cooperative behavior of magnetic microrobot swarms. *The International Journal of Robotics Research, 39*(5), 617–638.
35. Yan, J., Han, M., Zhang, J., Xu, C., Luijten, E. & Granick, S. (2016). Reconfiguring active particles by electrostatic imbalance. *Nature Materials, 15*(10), 1095–1099.
36. Zhang, B., Sokolov, A., & Snezhko, A. (2020). Reconfigurable emergent patterns in active chiral fluids. *Nature Communications, 11*(1), 1–9.
37. Leunissen, M. E., Vutukuri, H. R., & van Blaaderen, A. (2009). Directing colloidal self-assembly with biaxial electric fields. *Advanced Materials, 21*(30), 3116–3120.
38. Singh, D.P., Choudhury, U., Fischer, P. & Mark, A.G. (2017). Non-equilibrium assembly of light-activated colloidal mixtures. *Advanced Materials, 29*(32), 1701328.
39. Klajn, R., Wesson, P.J., Bishop, K.J. & Grzybowski, B.A. (2009). Writing self-erasing images using metastable nanoparticle "inks". *Angewandte Chemie International Edition, 48*(38), 7035–7039.
40. Liu, W., Chen, X., Lu, X., Wang, J., Zhang, Y. & Gu, Z. (2020). From passive inorganic oxides to active matters of micro/nanomotors. *Advanced Functional Materials, 30*(39), 2003195.
41. Melde, K., Mark, A.G., Qiu, T. & Fischer, P. (2016). Holograms for acoustics. *Nature, 537*(7621), 518–522.
42. Ahmed, D., Baasch, T., Blondel, N., Läubli, N., Dual, J. & Nelson, B.J. (2017). Neutrophil-inspired propulsion in a combined acoustic and magnetic field. *Nature Communications, 8*(1), 1–8.
43. Chen, Y., Ding, X., Steven Lin, S.C., Yang, S., Huang, P.H., Nama, N., Zhao, Y., Nawaz, A.A., Guo, F., Wang, W. & Gu, Y. (2013). Tunable nanowire patterning using standing surface acoustic waves. *ACS Nano, 7*(4), 3306–3314.

44. Keya, J.J., Suzuki, R., Kabir, A.M.R., Inoue, D., Asanuma, H., Sada, K., Hess, H., Kuzuya, A. & Kakugo, A. (2018). DNA-assisted swarm control in a biomolecular motor system. *Nature Communications, 9*(1), 1–8.
45. Theurkauff, I., Cottin-Bizonne, C., Palacci, J., Ybert, C. & Bocquet, L. (2012). Dynamic clustering in active colloidal suspensions with chemical signaling. *Physical Review Letters, 108*(26), 268–303.
46. Van Reenen, A., de Jong, A.M., den Toonder, J.M. & Prins, M.W. (2014). Integrated lab-on-chip biosensing systems based on magnetic particle actuation–a comprehensive review. *Lab on a Chip, 14*(12), 1966–1986.
47. Choi, J., Jeong, S., Cha, K., Qin, L., Li, J., Park, J. & Park, S. (2010). Positioning of microrobot in a pulsating flow using EMA system. *In 2010 3rd IEEE RAS & EMBS International Conference on Biomedical Robotics and Biomechatronics* (pp. 588–593). IEEE.
48. Vrooijink, G.J., Abayazid, M., Patil, S., Alterovitz, R. & Misra, S. (2014). Needle path planning and steering in a three-dimensional non-static environment using two-dimensional ultrasound images. *The International Journal of Robotics Research, 33*(10), 1361–1374.